Available online at www.sciencedirect.com
ScienceDirect
Trans. Nonferrous Met. Soc. China 35(2025) 3886−3901
Transactions of Nonferrous Metals Society of China
www.tnmsc.cn

Behavior of high-arsenic copper feed mixture in suspension smelting processes

Yu-jie CHEN[1], Yan-jie LIANG[2,3], Hui LIU[2,3], Pekka TASKINEN[4], Ari JOKILAAKSO[4], Zhun-qin DONG[5], Zhong-bing WANG[6], Tao CHEN[5]

1. School of Biological and Chemical Engineering, Nanyang Institute of Technology, Nanyang 473000, China;
2. School of Metallurgy and Environment, Central South University, Changsha 410083, China;
3. Chinese National Engineering Research Center for Control & Treatment of Heavy Metal Pollution, Changsha 410083, China;
4. School of Chemical Engineering, Aalto University, Espoo 00076, Finland;
5. Shandong Humon Smelting Co., Ltd., Yantai 264000, China;
6. School of Environment and Chemistry, Nanchang Hangkong University, Nanchang 330063, China

Received 1 November 2024; accepted 8 September 2025

Abstract: The suspension stage of copper flash smelting was examined by roasting a high arsenic copper smelting feed mixture at 500−900 °C for 0−20 s in nitrogen and air atmospheres. The enrichment of copper, lead, zinc, arsenic, and sulfur in the quenched calcine was determined via chemical analyses. Pyrite and chalcopyrite were the main minerals in the feed mixture, and about 55 wt.% of arsenic was in tennantite. The stability of the feed and the formation of S_2 and SO_2 during roasting were surveyed by thermal analysis combined with mass spectrometry. Selected pure impurity sulfides were studied for reference purposes. Results indicated that arsenic was released more easily in inert atmosphere compared to air, in which oxidation products of sulfides captured the released gaseous arsenic. Kinetics analyses showed that the third-order chemical reaction and three-dimensional diffusion models were found as the most suitable mechanism functions of arsenic volatilization in inert and air atmospheres, respectively.

Key words: complex concentrates; copper smelting; flash smelting; volatilization; kinetic modelling

1 Introduction

The copper content in the Earth's crust is approximately 0.01 wt.% [1], occurring mainly in various sulfide minerals, such as $CuFeS_2$ and Cu−S compounds. Arsenic-containing minerals are commonly found in copper, lead, zinc, and gold ores. Complex copper concentrates containing arsenic include minerals such as arsenopyrite (FeAsS), enargite (Cu_3AsS_4), tennantite ($(Cu,Fe)_{12}As_4S_{12}$), and lautite (CuAsS) [2−4]. The clean high-grade copper concentrates have been declining over decades [5−7]. With the growing demand for copper, various concentrates with high contents of harmful elements have gradually become common in copper extracting processes. Among these, high arsenic copper concentrates are particularly common, leading to an increase in arsenic-containing pollutants and by-products [8−11].

Two major methods are used to extract copper from ores: hydrometallurgy and pyrometallurgy. Hydrometallurgy is performed at or near room

Corresponding author: Hui LIU, Tel: +86-731-88576364, E-mail: liuhuicsu@163.com;
Pekka TASKINEN, Tel: +358-40-5017411, E-mail: pekka.taskinen@aalto.fi
https://doi.org/10.1016/S1003-6326(25)66919-6

temperature, offering advantages such as saving fuel and no slag generation. However, hydrometallurgy also has several inherent limitations, including equipment corrosion, challenging solid−liquid separation, and low leaching efficiency [12,13]. Therefore, the extraction of copper is predominantly based on pyrometallurgy [14−17]. Bath smelting and suspension smelting are the dominant modern copper smelting technologies [18,19].

During smelting, most arsenic in the feed volatilizes into the gas phase and reports to the flue dust. Because of the high copper grade in flue dusts, the arsenic-containing flue dusts are mixed back to the feed-mixture, which increases the arsenic content in the smelting furnace [20]. Several studies have investigated the effects of arsenic on copper smelting [21,22], its distribution behavior [23−25], and its speciation in copper flue dusts [20,26−28]. However, there is limited information available on the thermal behavior of arsenic during the suspension stage in the smelting vessel [29].

When the smelting feed is introduced into suspension smelting or bath smelting furnace, the feed particulates are rapidly heated before contacting the molten bath. Once the temperature reaches the boiling point of arsenic-containing phases [30], these phases volatilize into the gas phase and are discharged from the smelting furnace with the off-gas, forming arsenic-containing flue dust. Therefore, it is of great significance for the copper smelting industry to understand the thermal behavior of arsenic in the copper smelting feed within gas-particle suspensions.

The aim of this work is to simulate the suspension oxidation process by roasting a high arsenic copper smelting feed under nitrogen and air atmospheres at temperatures of 500−900 °C. The quenched calcines were analyzed to examine the enrichment degrees of elements and the volatilization kinetics of arsenic in the high-arsenic smelting feed in the suspension smelting process.

2 Experimental

2.1 Materials

The high-arsenic copper smelting feed (HB) used in this study was obtained from a copper smelter employing the bottom-blowing bath smelting process in Shandong province, China. The elemental composition was analyzed using inductively coupled plasma-optical emission spectroscopy 5100 (ICP-OES, Agilent, USA), an elemental analyzer Vario EL Cube (EA, Elementar, Germany), and an X-ray fluorescence spectrometer 1800 (XRF; Jindao, Japan) with Rh anode radiation and a standard slit at 36.5 °C. Copper, iron, sulfur and silicon were the major elements (Table 1), collectively accounting for more than 65 wt.% of the feed. In addition, arsenic, lead and zinc accounted for 2.0, 2.3, and 2.1 wt.% of the feed, respectively.

Mineralogical characteristics of HB were analyzed by a Mineral Liberation Analyzer FEI MLA 650 (Thermo Fischer Scientific, USA) equipped with a FEI Quanta 650 scanning electron microscope (SEM, Thermo Fischer Scientific, USA) and an energy dispersive spectrum analyzer Quantax 200 with Dual XFlash 5010 (EDS; Bruker, Germany). The FEI MLA 3.1 software package (Thermo Fischer Scientific, USA) [20] and its mineral standards library were used to determine the distribution of copper, iron and arsenic in the feed. The mineral liberation results are presented in Fig. 1 and Table S1 of Supplementary Material (SM), respectively.

As shown in Fig. 1, the HB particles exhibited irregular shapes and a non-uniform size distribution. Large particles contained multiple minerals, such as chalcopyrite, quartz, covellite, and sphalerite. Tennantite and tetrahedrite were not liberated from each other, while quartz and galena were found associated with pyrite. Table S1 in SM shows the mineral composition of HB. The main minerals were pyrite (27.3 wt.%) and chalcopyrite (17.3 wt.%),

Table 1 Elemental composition of high-arsenic copper smelting feed (wt.%)

Cu[1]	Fe[1]	As[1]	Zn[1]	Pb[1]	Sb[1]	Bi[1]	Al[1]	S[2]	Si[3]	Na[3]	Mg[3]	K[3]	Ca[3]	Others
17.0	25.3	2.0	2.3	2.1	0.6	0.1	1.0	26.5	9.5	0.5	1.8	0.6	1.8	8.9

[1]: ICP-OES; [2]: EA; [3]: XRF

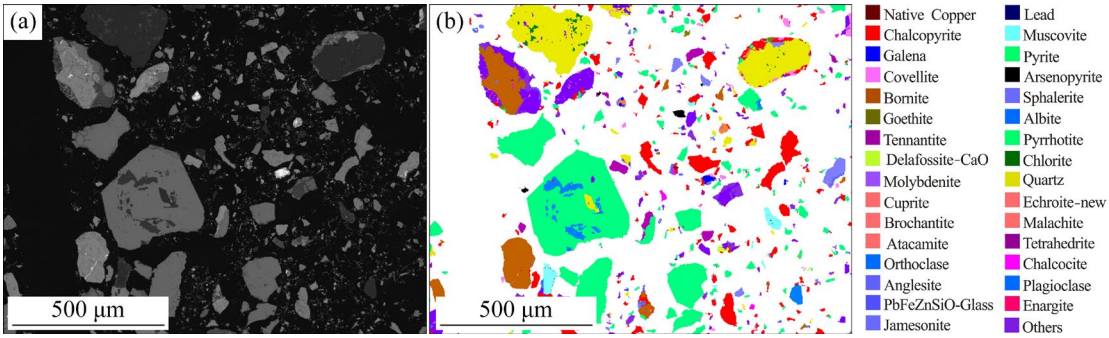

Fig. 1 Mineral liberation characteristics of HB: (a) Backscattered electron (BSE) image; (b) Analysis chart of final mineral liberation analyzer (MLA)

and the content of other minerals was less than 6 wt.%.

The distributions of copper, iron and arsenic in HB (analyzed by MLA) are shown in Table S2 of SM. More than 91 wt.% of copper was distributed in chalcopyrite (29.6 wt.%), chalcocite (21.0 wt.%), bornite (17.7 wt.%), tennantite (9.6 wt.%), covellite (7.9 wt.%), and native copper (6.0 wt.%). Iron mainly existed in pyrite, chalcopyrite, and magnetite. The main arsenic carrier in HB was tennantite, with additional arsenic present in arsenopyrite and reverts. Pure sulfide minerals (pyrite (FeS_2), arsenopyrite (FeAsS), chalcocite (Cu_2S), chalcopyrite ($CuFeS_2$) and bornite (Cu_5FeS_4)) used as reference materials were obtained from a Chinese industrial company, with a purity of >95%. The minerals were identified by a D/Max 2500 VB + 18 kW X-ray diffractometer (XRD; Rigaku, Japan) with Cu radiation (40 kV, 300 mA), a step size of 0.02°, and a scanning speed of 10 (°)/min over the 2θ range from 10° to 80°, as shown in Fig. S1 of SM.

Thermogravimetric analysis (TG) was performed using a NETZSCH-449F3 instrument (Netzsch, Germany) coupled online with a mass spectrometer (MS, NETZSCH-QMS403, Netzsch, Germany) to analyze the thermal behavior of HB and the composition of off-gases. Thermal analysis of the pure sulfides was performed using a thermogravimetry-differential scanning calorimetry (TG-DSC, NETZSCH-STA449C, Netzsch, Germany). Approximately 10 mg of each sample was placed in an alumina crucible. Measurements were conducted under a flow of air or argon (50 mL/min) at a heating rate of 10 °C/min.

2.2 Apparatus

The suspension process was simulated using a vertical furnace (Lenton PTF 15/45/450, UK), as illustrated in Fig. 2. The furnace was equipped with SiC heating elements and an impervious alumina working tube. The internal temperature was divided into three heating zones, which were controlled by Eurotherm 3216 proportional-integral-derivative (PID) controllers. A calibrated S-type Pt/90 pct Pt-10 pct Rh thermocouple (Johnson-Matthey Noble Metals, UK) with a maximum deviation from the standard of ±3°C was inserted into the working tube from the top to monitor the sample temperature. The thermocouple was connected to a 2010 DMM multimeter (Keithley, USA). The cold junction temperature was measured by a PT100 resistance thermometer (SKS Group, Finland) connected to a 2000 DMM multimeter (Keithley, USA). A National Instruments (NI) LabVIEW data logging program was used to collect temperature data throughout the experiments. Gas flow rates were regulated by DFC26 digital mass-flow controllers (Aalborg, USA).

2.3 Procedure

HB was dried in an oven in air at 90 °C for 24 h. Prior to the experiments, the temperature profile inside the working tube was measured to identify the hot zone within the range of 500−900 °C.

For each experiment, approximately 0.2 g of HB powder was placed into a platinum crucible. The crucible containing the sample was then placed in a platinum basket, which was suspended in the center of the furnace tube using a platinum wire. Initially, the crucible−sample−basket was inserted into the cold zone of the furnace. The lower end of the furnace working tube was sealed with a rubber plug, and the exhaust gas was directed to an

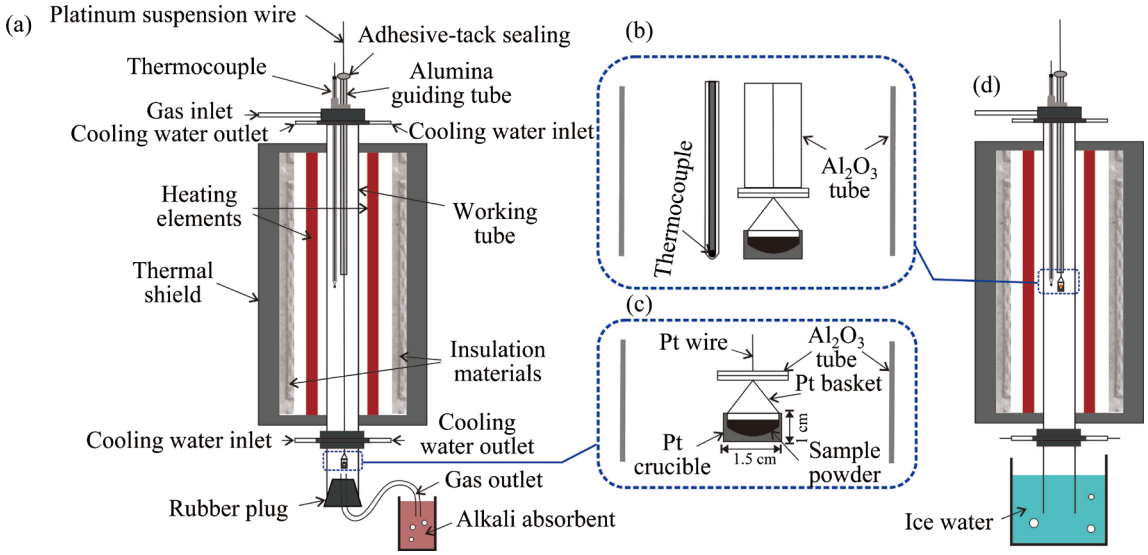

Fig. 2 Schematic diagram of vertical tube furnace (a, d) and detail of zone (b, c) used for experiments

absorption bottle filled with an alkali absorbent (Fig. 2(a)). Argon (Aga Linde, Finland, 99.999% purity) was introduced at a specified flow rate for 30 min to stabilize the atmosphere.

Subsequently, the platinum basket was lifted up to the hot zone and held there for a preset duration of 0−20 s. Before lifting, the rubber plug was removed in the ice−water mixture in the quenching vessel (Fig. 2(d)). After that, the specimen was dropped into the ice−water mixture for rapid quenching.

When investigating the influence of air atmosphere, the furnace tube was kept open, and a water quenching vessel was placed under the low temperature zone without direct contact with the furnace tube. The sample was then processed following the same procedure as described above. Each group of experiments was repeated 6−9 times to minimize random errors.

2.4 Kinetic analysis

Kinetic data obtained at 500 and 900 °C were analyzed to investigate the changes in copper, iron, zinc, arsenic and lead contents under air and inert atmospheres, and to determine the associated kinetic model parameters.

The kinetic parameters were evaluated employing a model-fitting method [31,32] based on the Arrhenius formula, which can be expressed in the following forms, as shown in Eqs. (1)−(3):

$$k=A\exp[-E/(RT)] \tag{1}$$

$$\ln k=\ln A-\frac{E}{RT} \tag{2}$$

$$\frac{\mathrm{d}\ln k}{\mathrm{d}T}=\frac{E}{RT^2} \tag{3}$$

where T is the thermodynamic temperature; k and A represent the reaction rate constant and the pre-exponential factor (frequency factor) at temperature T, respectively; E stands for the activation energy; R is the molar gas constant, 8.314 J/(mol·K).

The enrichment degree of each element in the calcine under different conditions was calculated using Eq. (4). Since iron is non-volatile under the experimental conditions, the element concentrations in the calcine were normalized using Eqs. (5) and (6). Consequently, the volatilization degree of arsenic from the feed, denoted as α, was defined by Eq. (7) and calculated according to Eq. (8). By combining Eqs. (4)−(6), the relationship between the arsenic enrichment degree (η_{As}) and its volatilization degree (α) was derived, as presented in Eq. (9):

$$\eta_i=\frac{m_1C_{i1}}{m_0C_{i0}} \tag{4}$$

$$m_0C_{Fe0}=m_1C_{Fe1} \tag{5}$$

$$\eta_i=\frac{C_{Fe0}}{C_{Fe1}}\frac{C_{i1}}{C_{i0}} \tag{6}$$

$$\frac{\mathrm{d}\alpha}{\mathrm{d}t}=kf(\alpha)=A\exp[-E/(RT)]\cdot f(\alpha) \tag{7}$$

$$\alpha=1-\frac{m_1 C_{\mathrm{As1}}}{m_0 C_{\mathrm{As0}}} \tag{8}$$

$$\alpha=1-\eta_{\mathrm{As}} \tag{9}$$

where η_i is the enrichment degree of element i in the quenched calcine; m_0, m_1, C_{i0} and C_{i1} represent the mass and the mass fraction of element i of HB before and after calcination, respectively; $f(\alpha)$ stands for the differential form of the reaction model; t is the time.

The total concentrations of copper, iron, zinc, arsenic, and lead in the quenched calcines were determined using a wet digestion technique following US Environmental Protection Agency guidelines (USEPA, Method 3052). The metal concentrations were determined by ICP-OES and the sulfur content was measured by EA. To minimize random errors, each specimen was divided into three subsamples for independent analysis, and the average values are reported.

$$G(\alpha)=\int_0^{\alpha}\frac{\mathrm{d}\alpha}{f(\alpha)}=\int_0^{t}A\exp\left(-\frac{E}{RT}\right)\mathrm{d}t=kt \tag{10}$$

The integral form of the reaction model, $G(\alpha)$, can be obtained by integrating the reciprocal of the reaction model function $f(\alpha)$ with respect to α based on the reaction rate equation in Eq. (7), as shown in Eq. (10).

The gas−solid reaction kinetic models and their corresponding $G(\alpha)$ functions tested in this work are listed in Table 2. For isothermal conditions, $G(\alpha)$ and k can be determined by linear fitting of the experimental data. The corresponding values of E/T and $\ln A$ can be calculated from the slope and intercept of the fitted linear regression of $\ln k$ versus T^{-1}, in accordance with Eqs. (1) and (2). This procedure allows for the determination of the kinetic parameters E and A.

Table 2 Gas−solid reaction kinetic models [33−36]

Reaction model	Code	$G(\alpha)$
Nucleation and growth model	Power law (P2)	$\alpha^{1/2}$
	Power law (P3)	$\alpha^{1/3}$
	Avrami-Erofe'ev Eq. (1) (A2)	$[-\ln(1-\alpha)]^{1/2}$
	Avrami-Erofe'ev Eq. (2) (A3)	$[-\ln(1-\alpha)]^{1/3}$
	Avrami-Erofe'ev Eq. (3) (A4)	$[-\ln(1-\alpha)]^{1/4}$
Geometrical contraction model	Contraction area (R2)	$1-(1-\alpha)^{1/2}$
	Contraction area (R3)	$1-(1-\alpha)^{1/3}$
Diffusion model	1D Diffusion (D1)	α^2
	2 D Diffusion (D2)	$\alpha+(1-\alpha)]\ln(1-\alpha)$
	3 D Diffusion (D3)	$[1-(1-\alpha)^{1/3}]^2$
	4 D Diffusion (D4)	$(1-2\alpha/3)-(1-\alpha)^{2/3}$
Reaction-order model	Zero-order (F0/R1)	α
	First-order (F1)	$-\ln(1-\alpha)$
	Second-order (F2)	$(1-\alpha)^{-1}-1$
	Third-order (F3)	$0.5[(1-\alpha)^{-2}-1]$

3 Results and discussion

3.1 Thermal behavior of pure sulfide minerals

3.1.1 Sulfide minerals in inert atmosphere

The TG-DSC curves of pure pyrite, chalcocite, bornite, chalcopyrite, and arsenopyrite minerals under a flowing argon atmosphere (50 mL/min) are shown in Fig. 3. These minerals represent the major mineral phases identified in the HB, as presented in Table S1 of SM.

As shown in Fig. 3(a), the thermal decomposition of pyrite in argon initiated when the temperature exceeded 460 °C [37]. The first decomposition stage of pyrite completed at approximately 551 °C, accompanied by an endothermic peak at 521 °C in the DSC curve and a mass loss of 3.5 wt.%. This can be assigned to the conversion of pyrite to pyrrhotite, as described by Eq. (11) [38]. The second endothermic peak at 640 °C can be ascribed to the secondary decomposition of pyrite forming the stoichiometric iron sulfide (FeS), i.e., pyrrhotite, according to Eq. (12). With further increase in temperature, FeS released S_2(g) and formed elemental iron, as represented by Eq. (13):

$$(1-x)\mathrm{FeS_2}=\mathrm{Fe_{1-x}S}+(0.5-x)\mathrm{S_2(g)} \tag{11}$$

$$\mathrm{Fe_{1-x}S}=(1-x)\mathrm{FeS}+0.5x\mathrm{S_2(g)} \tag{12}$$

$$2\mathrm{FeS}=2\mathrm{Fe}+\mathrm{S_2(g)} \tag{13}$$

TG-DSC curves of chalcocite are presented in Fig. 3(b). The DSC trace exhibited four small endothermic peaks at 99, 423, 506, and 860 °C. Correspondingly, the TG curve showed a total mass loss of 4.7 wt.% in the temperature range of

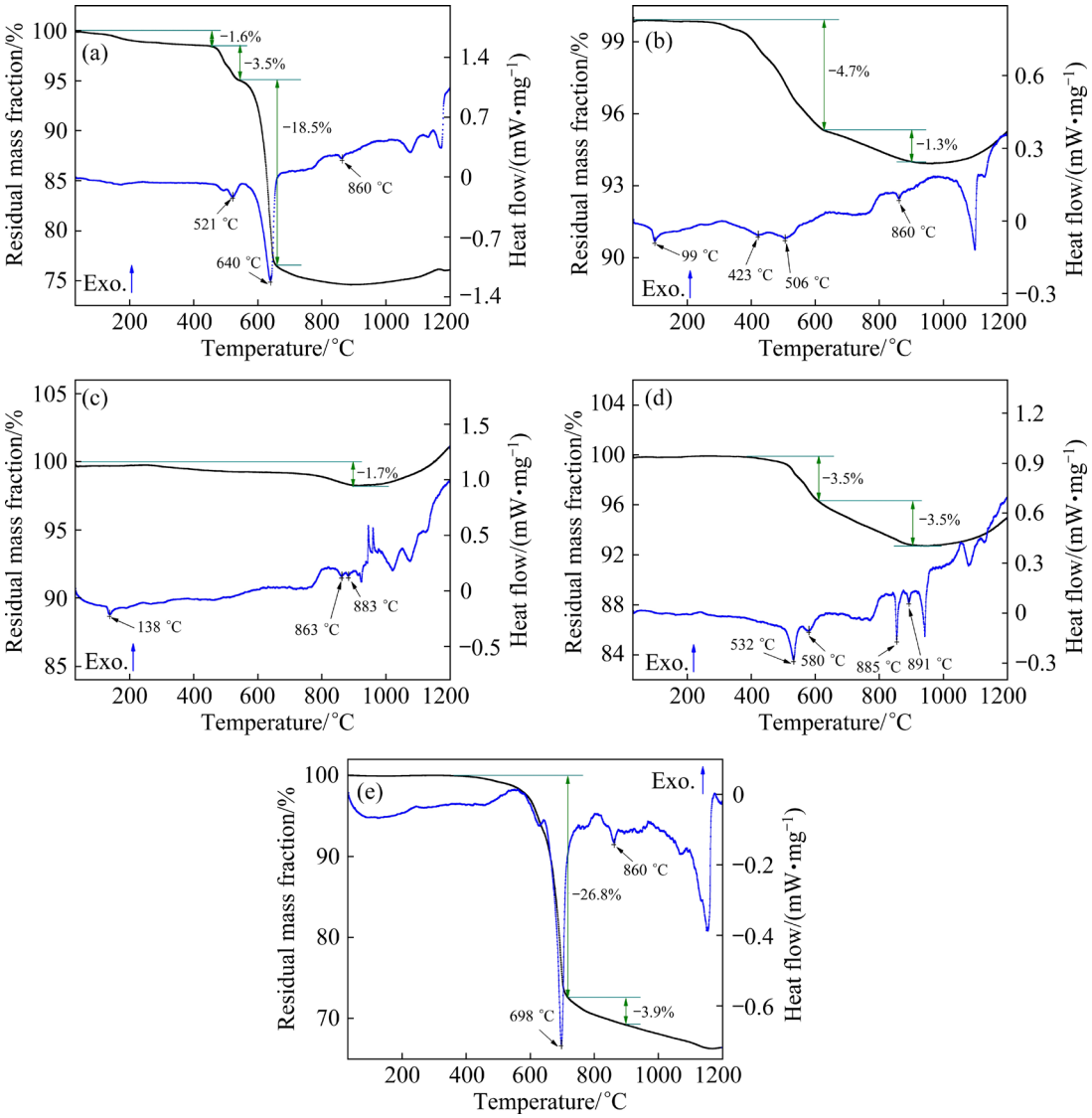

Fig. 3 Thermal analyses of pyrite (a), chalcocite (b), bornite (c), chalcopyrite (d), and arsenopyrite (e) minerals in argon

30−623 °C, followed by an additional 1.3 wt.% mass loss up to 900 °C. The endothermic peak at 99 °C can be attributed to the release of H_2O (g). As indicated by the XRD pattern of the pure chalcocite mineral (Fig. S1(e) of SM), a small amount of pyrite was present. Therefore, the endothermic peaks at 423 and 506 °C can be assigned to the first two decomposition stages of pyrite (Eqs. (11) and (12)). The second mass-loss stage, observed at 660−900 °C, is consistent with the behavior of pyrite shown in Fig. 3(a).

As seen in Fig. 3(c), bornite underwent a slight mass loss at 30−900 °C, which can be attributed to release both of H_2O (g) and a small amount of S_2(g).

Figure 3(d) shows the TG-DSC results for chalcopyrite. The TG curve indicated a continuous mass loss in the temperature range of 400−900 °C, which can be divided into two distinct steps. The first step, with a mass loss of 3.5 wt.%, was attributed to the release of S_2(g) due to the transformation of chalcopyrite to β-chalcopyrite, as represented by Eq. (14) [39]. The second mass loss can be explained by the decomposition of β-chalcopyrite (Eq. (15)) and the evaporation of sulfur from bornite and FeS.

$$2CuFeS_2=2CuFeS_{2-x}+xS_2(g) \quad (14)$$

$$10CuFeS_{2-x}=2Cu_5FeS_4+8FeS+(2-5x)S_2(g) \quad (15)$$

As shown in Fig. 3(e), the TG curve of arsenopyrite exhibited a significant mass loss at 390−710 °C, followed by a gradual mass loss up to 900 °C. An endothermic peak appeared at 698 °C in the DSC curve can be assigned to the

decomposition of arsenopyrite and the release of $As_2(g)$ (Eq. (16)). The second stage of mass loss was consistent with the behavior observed for pyrite (Fig. 3(a)).

$$2FeAsS=2FeS+As_2(g) \quad (16)$$

3.1.2 Sulfide minerals in air

Typical TG-DSC curves for the oxidation of pyrite, chalcocite, bornite, chalcopyrite, and arsenopyrite in air are shown in Fig. 4. It can be seen in Fig. 4(a) that pyrite continued to lose mass in the ranges of 427−559 °C and 559−694 °C, with corresponding mass losses of 11.9 wt.% and 19.7 wt.%, respectively. The DSC curve exhibited a distinct exothermic peak at 474 °C. Therefore, the mass loss at 427−559 °C can be attributed to the oxidation of pyrite, forming hematite and releasing $SO_2(g)$, as described by Eq. (17). In the temperature range of 559−694 °C, intermediate products such as pyrrhotite, hematite, and ferric sulfate were formed and subsequently converted into hematite [40,41].

$$4FeS_2+11O_2(g)=2Fe_2O_3+8SO_2(g) \quad (17)$$

The TG curve of chalcocite in air from 30 to 1200 °C (Fig. 4(b)) shows an mass increase at 334−685 °C, followed by a decrease from 685 to 1200 °C. The mass increasing stage can be divided into two parts. The first stage (334−531 °C) was assigned to surface oxidation of chalcocite particles, forming copper (I) oxide and copper sulfate. The second stage (548−685 °C) can be linked with continuous oxidation of the residual sulfide, generating copper oxide and copper sulfate.

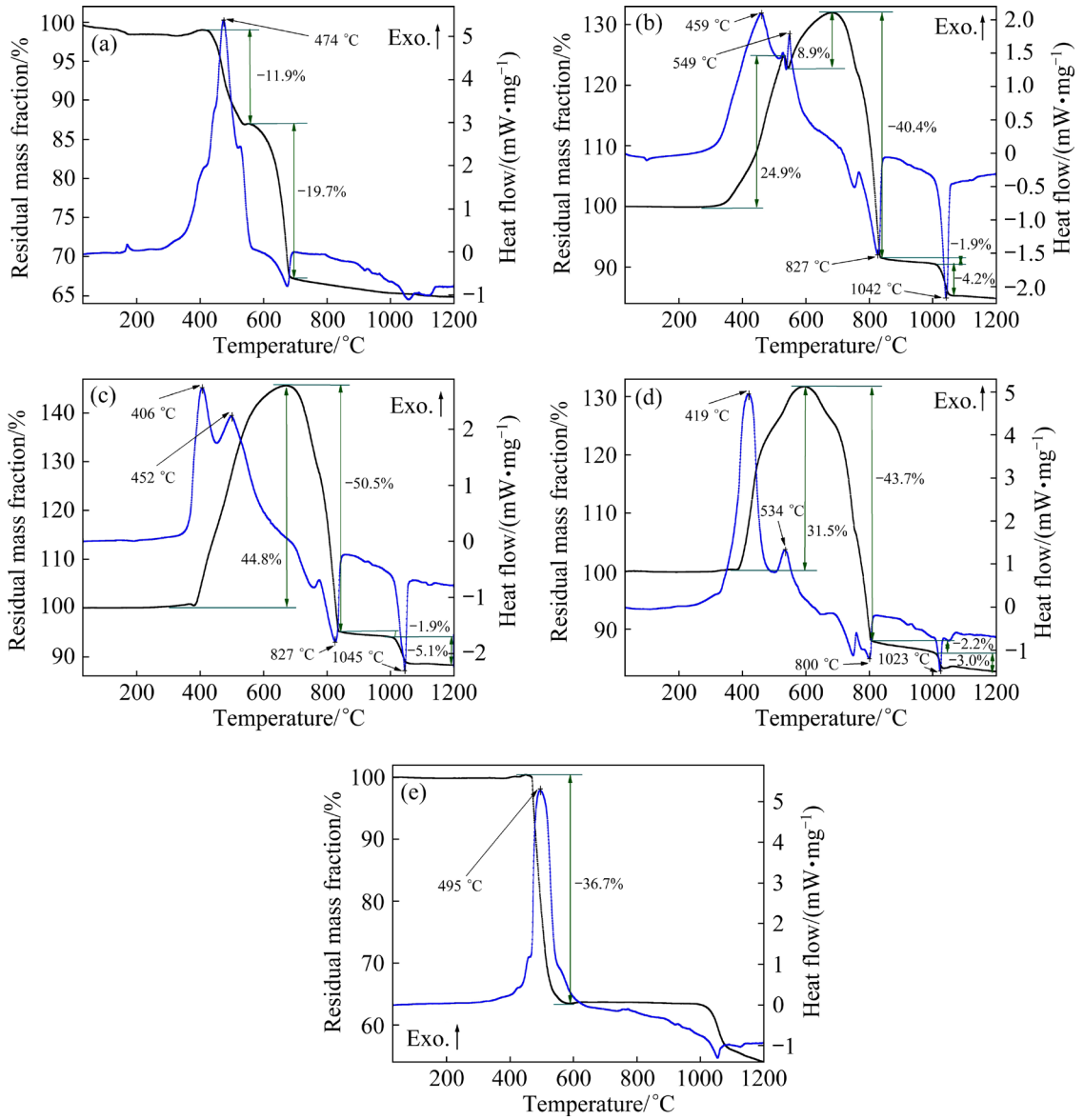

Fig. 4 Thermal analyses of pyrite (a), chalcocite (b), bornite (c), chalcopyrite (d), and arsenopyrite (e) minerals in air

Two exothermic peaks appeared in the DSC curve at 459 and 549 °C, both associated with oxidation processes. Nevertheless, a momentary mass loss accompanied by an exothermic process occurred at 531−548 °C, indicating complete oxidation of the chalcocite surfaces. The formed copper sulfate scale covered the chalcocite surface, preventing the penetration of air into the chalcocite core. This led to slightly more SO_3(g) released from decomposition of copper sulfate (Eq. (18)) than absorbed O_2(g) [39]. The mass loss at 685−839 °C was due to decomposition of copper sulfate [42], and the mass change from 839 to 1000 °C was minimal.

$$2CuSO_4=CuO\cdot CuSO_4+SO_3(g) \quad (18)$$

The TG curves of bornite (Fig. 4(c)), chalcopyrite (Fig. 4(d)) and covellite [43] in air at 30−1200 °C exhibited trends similar to that of chalcocite (Fig. 4(b)). In air, the oxidation reactivity of these minerals followed the order of chalcocite, covellite, chalcopyrite and bornite [3].

As shown in Fig. 4(e), arsenopyrite underwent a significant mass loss of 36.7 wt.% during heating. An exothermic peak was observed in the DSC curve at 495 °C, with an onset temperature of 468 °C. This can be attributed to the oxidation of arsenic in arsenopyrite releasing As_2O_3(g) and SO_2(g).

3.2 Thermal behavior of high-arsenic copper smelting feed

3.2.1 HB in nitrogen

The TG-DSC curves of HB in nitrogen at 30−1300 °C are shown in Fig. 5(a), and the mass spectrum of the off-gas (monitoring $\langle S_2+SO_2\rangle$) is shown in Fig. 5(b). HB exhibited continuous mass from 30 to 1300 °C, which can be divided into three steps. The first stage, occurring at 30−380 °C, resulted in a mass loss of 1.7 wt.%. A weak endothermic peak appeared at 379 °C in the DSC curve, indicating that this mass loss can be ascribed to the removal of crystalline water.

The second stage, from 380 to 800 °C, exhibited a mass loss of 12.3 wt.%. The corresponding DSC curve showed endothermic peaks at 499, 543, 608 and 649 °C. According to the TG-DSC curve of pyrite in nitrogen atmosphere (Fig. 3(a)), the endothermic peaks at 499 and 649 °C were assigned to the two-stage decomposition of pyrite. From Figs. 3(a, b), it can be affirmed that the endothermic peak at 543 °C in Fig. 5(a) can be attributed to the decomposition of chalcopyrite, and the peaks at 608 and 649 °C were ascribed to chalcopyrite decomposition and the secondary decomposition of pyrite. These reactions resulted in the release of $\langle S_2+SO_2\rangle$ at 380−680 °C.

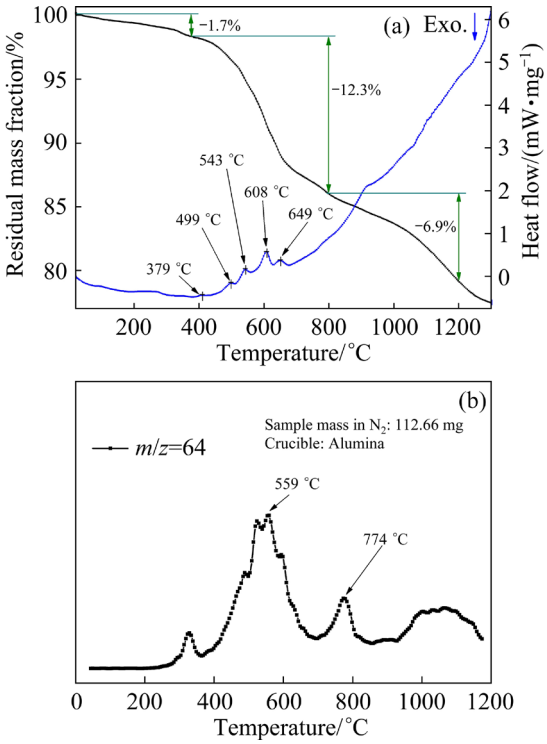

Fig. 5 TG-DSC curves of HB in N_2 (a) and in-suit mass spectra of S_2 and SO_2 released from HB in N_2 (b)

It can be seen in Fig. 5(b) that a certain amount of $\langle S_2+SO_2\rangle$ was released from HB at 680−710 °C. This phenomenon can be attributed to the release of S_2(g) and As_2(g) in the decomposition of arsenopyrite forming As_xS(g). After the complete decomposition of arsenopyrite, the continuous release of S_2(g) resulted in a distinct peak at 774 °C, as evident in Fig. 5(b).

The third mass loss stage (6.9 wt.%) occurred at 800−1200 °C. No significant endothermic or exothermic peaks were observed in the DSC curve.

3.2.2 HB in air

The TG-DSC curves of HB in air from 30 to 1300 °C are shown in Fig. 6(a), and the mass spectrometry data for $\langle S_2+SO_2\rangle$ in the off-gas are presented in Fig. 6(b).

As observed in Fig. 6(a), the mass change of HB with increasing temperature can be divided into four steps. In contrast to the behavior in nitrogen

atmosphere, HB did not lose mass but gained mass in the second stage (580−676 °C) in air. The DSC curve displayed two exothermic peaks at 520 and 598 °C, and two endothermic peaks at 742 and 976 °C. Figure 6(b) indicates that ⟨S_2+SO_2⟩ is released in two temperature ranges of 280−570 °C and 640−900 °C, with two prominent peaks in the MS curve at 463 and 758 °C, suggesting that maximum release occurred at 463 °C.

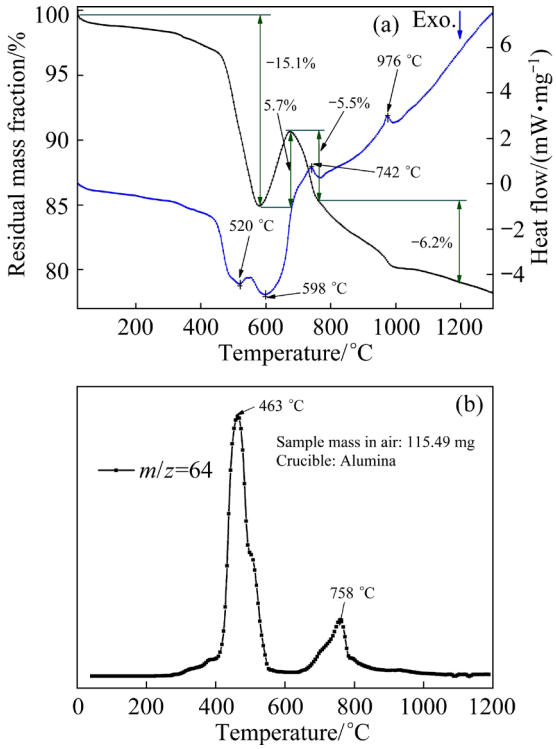

Fig. 6 TG-DSC curves of HB in air (a) and in-suit mass spectra of S_2 and SO_2 released from HB in air (b)

It can be inferred from Fig. 6 that the mass loss of HB in air (30−580 °C) was attributed to greater mass loss from sulfur release (from pyrite and arsenopyrite) than mass gain from oxidation of copper-bearing minerals. The mass gain at 580 and 676 °C was assigned to sulfation of oxidation products. The mass loss from 676 to 1000 °C was due to the release of sulfur trioxide during the decomposition of sulfates. The exothermic peaks at 520 and 598 °C, as well as endothermic peak at 742 °C, were associated with sulfation and decomposition reactions. The endothermic peak at 976 °C, which did not involve significant mass change, may be assigned to a phase transformation or melting process [44].

The residence time of concentrate in the reaction shaft of a flash smelting furnace is in the range of 2−3 s [45,46]. In single particle studies on sulfide minerals under residence time of similar magnitude to those in industrial furnaces, no sulfate formation was detected on partially oxidized and desulfurized grains [47]. This indicates that the formation kinetics of copper sulfates (within their thermal stability range of 500−1000 °C) is slower than the sulfide oxidation processes and formation of magnetite scales.

3.3 Enrichment of elements in calcine

3.3.1 Effect of temperature

The contents of copper, iron, arsenic, lead, zinc and sulfur in the quenched calcines of HB roasted in air at 500, 600, 700, 800 and 900 °C for 5, 10 and 20 s were analyzed, and their enrichment degrees were calculated using Eq. (6). The results are presented in Fig. 7.

As shown in Figs. 7(a, c, e), the enrichment degrees of arsenic in the quenched calcines decreased as the temperature increased from 500 to 900 °C in air. This indicates that a larger fraction of arsenic evaporated into the gas phase at higher temperatures. A similar trend was observed for sulfur. Based on these results, arsenic is more volatile than sulfur under the studied suspension oxidation process.

In the experiments, the volatilization of low-boiling-point elements such as arsenic and sulfur will increase the enrichment degrees of high-boiling-point phases to some extent i.e., copper, lead and zinc. As shown in Figs. 7(b, d, f), the enrichment degrees of copper, lead, and zinc exhibited increasing trends with rising temperature. After roasting at 900 °C for 20 s, the enrichment degrees reached approximately 107% for copper, 105% for lead, and 103% for zinc.

It can be concluded that during rapid heating process in suspension, less than 5 % of copper, lead and zinc volatilized and entered flue dust.

3.3.2 Effect of residence time

The enrichment degrees of copper, arsenic, lead, zinc and sulfur in the calcines roasted at 700, 800, and 900 °C under different residence time in air are shown in Fig. 8.

Figures 8(a, c, e) show that the enrichment degrees of arsenic in the calcines gradually decreased with extending time from 0 to 20 s, resulting in reductions of 12% at 700 °C, 14% at 800 °C, and 25% at 900 °C relative to the initial

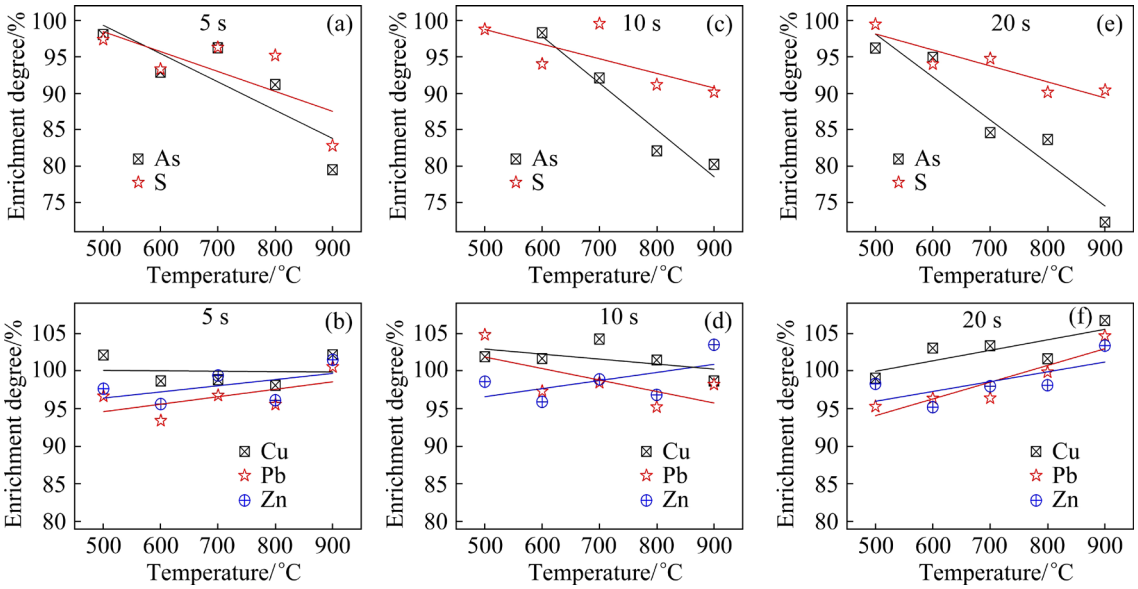

Fig. 7 Effect of roasting temperature on enrichment degrees of elements in quenched HB calcines in air: (a, c, e) As and S; (b, d, f) Cu, Pb and Zn

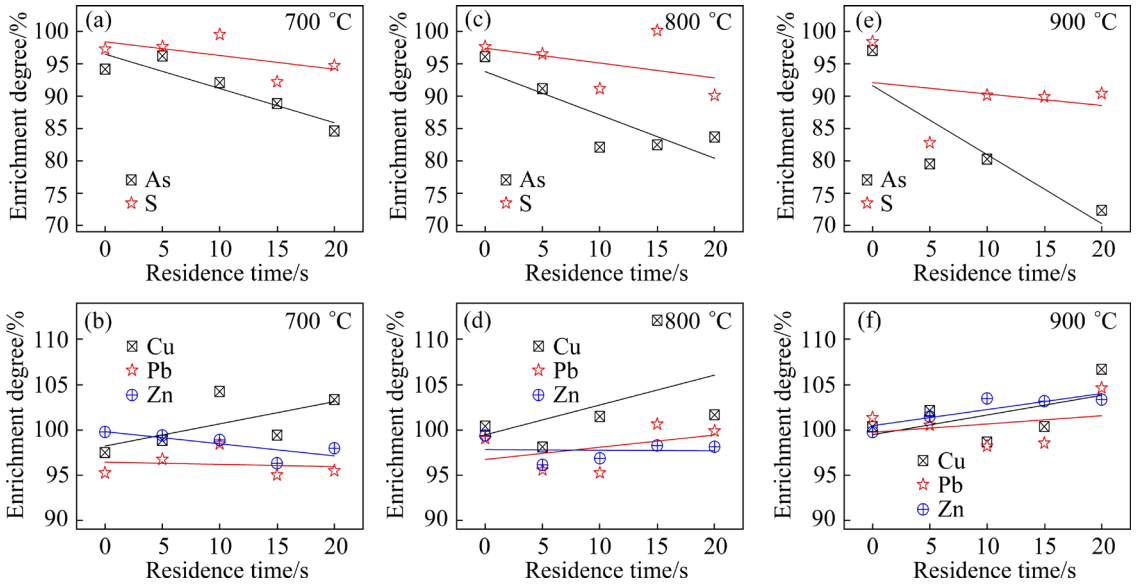

Fig. 8 Effect of residence time on enrichment degree of elements in quenched HB calcines in air: (a, c, e) As and S; (b, d, f) Cu, Pb and Zn

arsenic content. When HB was held in air at 900 °C for 20 s, the arsenic enrichment degree reached 72%. It can be inferred that extending the in-flight time enhances arsenic volatilization, thereby reducing arsenic content in the condensed smelting products. Similar to arsenic, the enrichment degree of sulfur tended to decrease with extending the residence time.

Notably, the enrichment degrees of arsenic and sulfur cannot reach 100% at 0 s, as complete dearsenification and desulfurization require sufficient time. When the platinum basket was manually lifted from the furnace bottom to the constant temperature zone, particles in HB underwent rapid heating. During this process, some low-boiling-point phases evaporated into the gas phases, causing localized fluctuations in element distribution. Thus, when HB was held at the designed temperatures for 0 s, the enrichment degrees of arsenic and sulfur remained below 100%.

As shown in Figs. 8(b, d, f), the enrichment degrees of copper, lead and zinc exhibited basically the same trend within the temperature range of

700−900 °C under oxidizing conditions. This consistency can be attributed to the use of an oxidative atmosphere, in which the oxidation products of these three elements, such as Cu_2O, PbO, and ZnO, had low vapor pressures at the experimental temperatures. The enrichment degree of zinc fluctuated slightly between 96% and 103%. The enrichment degrees of copper and lead varied within the ranges of 97%−112% and 95%−105%, respectively.

3.3.3 Effect of atmosphere

The enrichment degrees of copper, arsenic, lead, and zinc in the calcines at 500, 700, and 900 °C in air and argon are compared in Fig. 9.

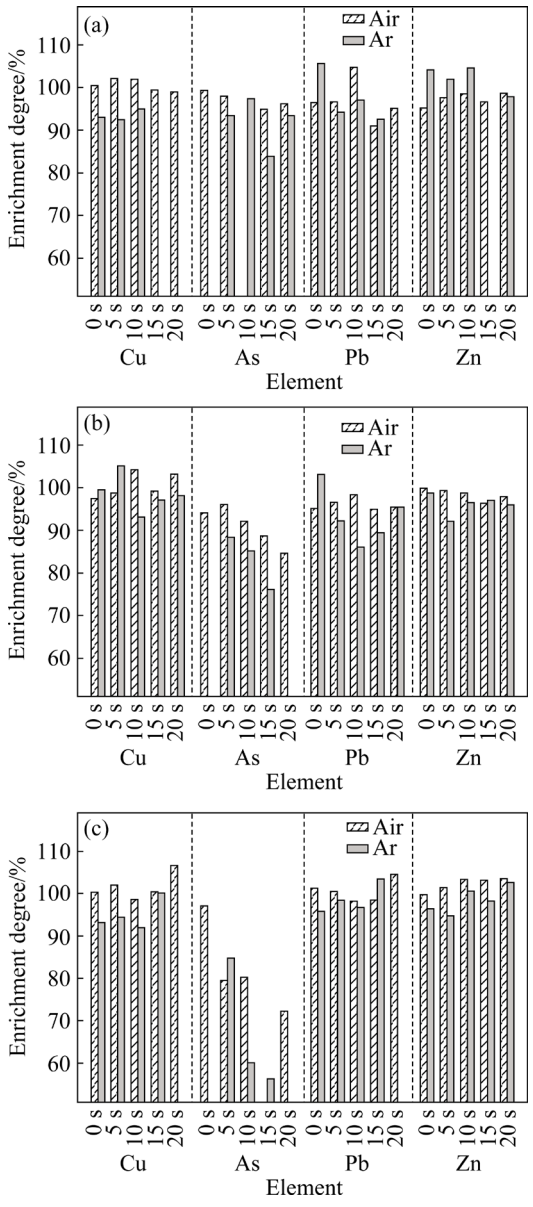

Fig. 9 Enrichment degrees of Cu, As, Pb, and Zn in quenched HB calcines: (a) 500 °C; (b) 700 °C; (c) 900 °C

Figure 9 shows that arsenic enrichment degrees in air are higher than those in argon at 500, 700, and 900 °C. This indicates that undecomposed arsenopyrite was gradually oxidized by oxygen in air, forming non-volatile arsenates. At elevated temperatures in an oxidative environment, the generated arsenic oxide reacted with oxidation products of metal sulfides i.e., magnetite, copper oxide, and sulfates to form arsenates. These subsequently blocked the pores of the calcines, thereby inhibiting arsenic volatilization. The relevant reactions are represented by Eqs. (19)−(24) [22,37,44].

$$FeAsS+3O_2(g)=FeAsO_4+SO_2(g) \quad (19)$$

$$4FeAsS+3O_2(g)=4FeS+2As_2O_3(g) \quad (20)$$

$$Fe_2O_3+As_2O_3(g)+O_2(g)=2FeAsO_4 \quad (21)$$

$$4Fe_3O_4+6As_2O_3(g)+7O_2(g)=12FeAsO_4 \quad (22)$$

$$39CuO+11As_2O_3(g)=4Cu_3As+9Cu_3(AsO_4)_2 \quad (23)$$

$$6CuSO_4+2As_2O_3(g)=2Cu_3(AsO_4)_2+6SO_2(g)+O_2(g) \quad (24)$$

Nevertheless, an argon atmosphere was more favorable for the decomposition of arsenic-containing sulfide minerals i.e., tennantite and arsenopyrite, and promoted the conversion of arsenic into low-boiling-point sulfides, as shown in Eqs. (25)−(27) [48−51]. Therefore, arsenic is more easily volatilized in the inert atmosphere.

$$2Cu_{12}As_4S_{13}=12Cu_2S+2As_4S_4(g)+3S_2(g) \quad (25)$$

$$2FeAsS=2FeS+As_2(g) \quad (26)$$

$$As_2(g)+S_2(g)=2AsS(g) \quad (27)$$

As shown in Fig. 9, the enrichment degrees of copper in air were slightly higher than those in argon, and the same trend was observed for lead. The enrichment degree of zinc in argon at 500 °C exceeded that in air. In contrast, at 700 and 900 °C, the enrichment degree of zinc in air became slightly higher than that in argon.

3.4 Arsenic volatilization kinetics

3.4.1 In inert atmosphere

The arsenic volatilization rates of HB in argon at temperatures ranging from 500 to 900 °C for different residence time were calculated using Eqs. (6) and (9). The results are shown in Fig. 10(a).The arsenic volatilization rates obtained at 900 °C in argon (Fig. 10(a)) were applied to the reaction kinetic models listed in Table 2 to establish

relationships between $G(\alpha)$ and t. The data were subjected to linear fitting, and the results are provided in Table S3 of SM. As shown in Table S3 of SM, the experimental arsenic volatilization rates at 900 °C in argon exhibited the highest correlation coefficient (R^2=0.9535) with the third-order chemical reaction model (F3) from Table 2. The slope of the fitted equation was 8.881×10^{-2}. Therefore, the integral kinetic function $G(\alpha)=0.5[(1-\alpha)^{-2}-1]$ presents the arsenic volatilization kinetic model of HB at 900 °C in argon, with a rate constant of $k_{HB-Ar,900}=8.88\times10^{-2}$.

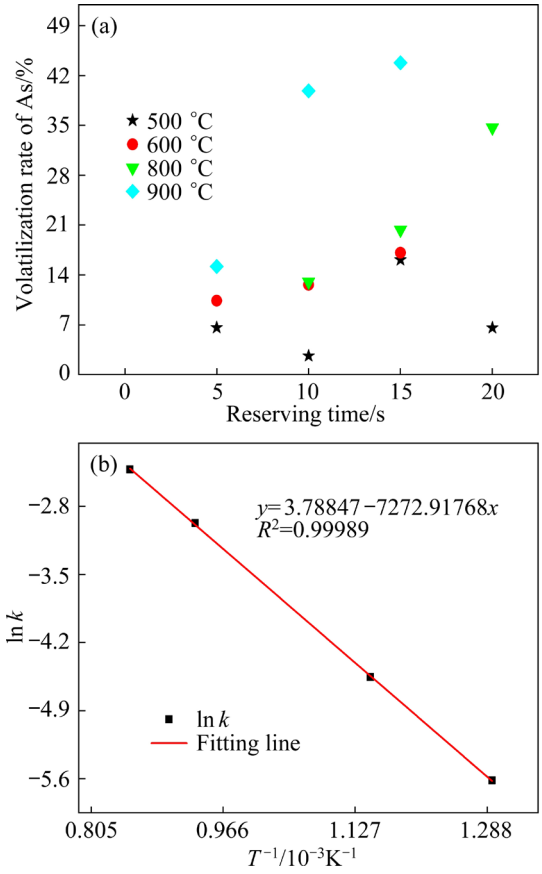

Fig. 10 Volatilization rate of arsenic in HB (a) and ln k vs $1/T$ plot for linear fitting (b) of arsenic volatilization in argon

The experimental arsenic volatilization data of HB at 500, 600, and 800 °C were substituted into the rate equation $G(\alpha)=0.5[(1-\alpha)^{-2}-1]$. By linearly fitting the relationship between $G(\alpha)$ and t, the rate constants of $k_{HB-Ar,500}$, $k_{HB-Ar,600}$, and $k_{HB-Ar,800}$ were obtained as 3.64×10^{-3}, 1.05×10^{-2}, and 5.11×10^{-2}, respectively.

Equation (2) corresponds to the Arrhenius equation, which describes a linear relationship between ln k and $1/T$. Thus, the calculated ln k and the corresponding $1/T$ were linearly fitted, as shown in Fig. 10(b). From the slope and intercept of the fitting line, the values of $-E/R$ and ln A were determined to be −7273 and 3.8, respectively. Using these values, E and A were calculated as 60.5 kJ/mol and 44.2 s^{-1}, respectively. Combining Eqs. (1) and (10), the kinetic mechanism function for arsenic volatilization from HB under non-oxidizing conditions was derived as

$$0.5[(1-\alpha)^{-2}-1]=44.189\exp[-60467/(RT)]\cdot t \quad (28)$$

3.4.2 In air atmosphere

The arsenic volatilization rates of HB in air at temperatures ranging from 500 to 900 °C for different residence time were calculated using Eqs. (6) and (9), with the results presented graphically in Fig. 11(a). The method for determining the volatilization kinetic mechanism function of arsenic in HB in air followed the same procedure as described in Section 3.4.1.

The linearly fitted results for arsenic volatilization in air and at 900 °C, based on the

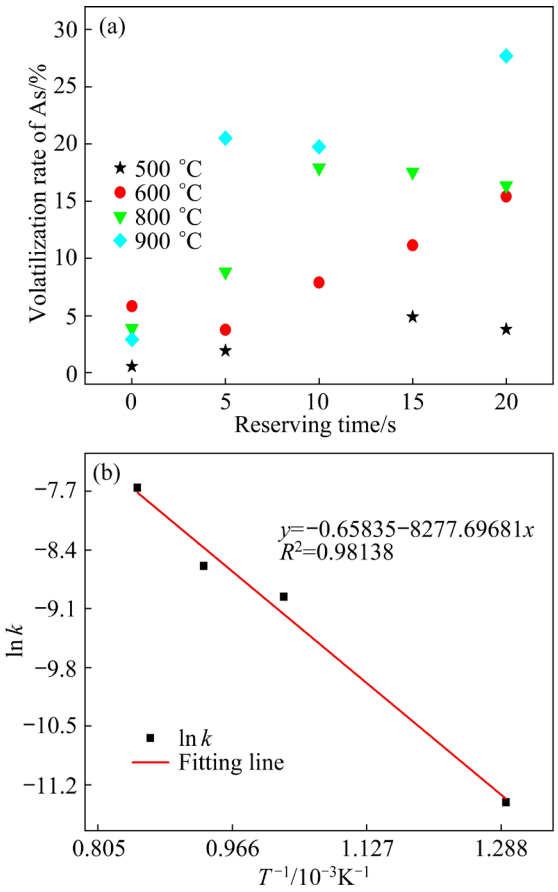

Fig. 11 Volatilization rate of arsenic in HB (a) and ln k vs $1/T$ plots for linear fitting (b) of arsenic volatilization in air

reaction kinetic models, are listed in Table S4 of SM. As shown in Table S4 of SM, the mechanism function of the three-dimensional diffusion model (D3) exhibited the best match, with a correlation coefficient of 0.9475. The slope of the fitted equation was 4.71×10^{-4}, corresponding to the rate constant $k_{HB-air,900}=4.71\times10^{-4}$. Similarly, the rate constants $k_{HB-air,500}$, $k_{HB-air,700}$, and $k_{HB-air,800}$ were determined as 1.11×10^{-5}, 1.29×10^{-4}, and 1.86×10^{-4}, respectively.

Figure 11(b) presents the linear relationship between ln k and $1/T$ at 500, 700, 800, and 900 °C. E and A were derived from the slope and intercept of the fitted line. The volatilization kinetic of arsenic in HB in air is thus described by Eq. (29).

$$[1-(1-\alpha)^{1/3}]^2=0.518\exp[-68821/(RT)]\cdot t \quad (29)$$

4 Conclusions

(1) In an inert atmosphere, the feed mixture exhibited continuous mass loss. In air, however, an initial mass gain occurred due to sulfide oxidation to sulfates and subsequent sulfate decomposition into oxides. Oxidation products also interacted with arsenic released at lower temperatures.

(2) Online mass spectrometry analysis of the off-gases confirmed that the release of $\langle S_2+SO_2\rangle$ from the feed was lower in inert atmosphere than in air.

(3) In air, arsenic was more volatile than sulfur during the suspension oxidation. Copper and lead showed slightly higher volatilization in air than in argon, similar to zinc except at 500 °C, where zinc volatilization in argon was slightly higher than that in air within 10 s.

(4) The arsenic volatilization rate from the feed can be enhanced by increasing temperature, extending the in-flight time, and reducing the oxygen potential. The kinetic mechanism functions for arsenic volatilization followed the third-order chemical model under inert atmosphere, and the three-dimensional diffusion model in air.

CRediT authorship contribution statement

Yu-jie CHEN: Data curation, Investigation, Writing − Original draft, Formal analysis, Project administration, Funding acquisition; **Yan-jie LIANG:** Formal analysis, Supervision; **Hui LIU:** Formal analysis, Funding acquisition, Writing − Review & editing; **Pekka TASKINEN:** Methology, Supervision, Writing − Review & editing; **Ari JOKILAAKSO:** Funding acquisition, Project administration, Supervision; **Zhun-qin DONG:** Investigation, Resources; **Zhong-bing WANG:** Formal analysis, Funding acquisition; **Tao CHEN:** Investigation, Resources.

Declaration of competing interest

The authors declare that they have no known competing financial interests or personal relationships that could have appeared to influence the work reported in this paper.

Acknowledgments

The authors gratefully acknowledge financial support from the Research Foundation for Doctor of Nanyang Institute of Technology, China (No. NGBJ-2022-27), the National Key Research and Development Program of China (No. 2023YFC3904002), the National Natural Science Foundation of China (Nos. 52064038, 52364056), the Science and Technology Research Project of Henan Province, China (No. 252102320113), the Key Scientific Research Project Plan of Colleges and Universities in Henan Province, China (No. 25B610009), and Jiangxi Provincial Natural Science Foundation, China (Nos. 20232BCJ22049, 20232ACB214009). This work utilized the Academy of Finland's RawMatTERS Finland Infrastructure (RAMI) based at Aalto University, GTK Espoo, and VTT Espoo.

Supplementary Materials

Supplementary Materials in this paper can be found at: https://tnmsc.csu.edu.cn/download/22-p3886-2024-1434-Supplementary_Materials.pdf.

References

[1] XU Bing-she, LI Zhao-ming. Metallurgy technology of copper [M]. 2nd ed. Beijing: Publishing House of Chemical Industry, 2006. (in Chinese)

[2] GOW R N, HUANG H, YOUNG C. Utility of mass-balanced EH-pH diagrams II: Stoichiometry of Cu−As−S−H_2O system [J]. Minerals and Metallurgical Processing, 2016, 33: 107−115.

[3] LONG G, PENG Yong-jun, BRADSHAW D. A review of copper−arsenic mineral removal from copper concentrates [J]. Minerals Engineering, 2012, 36/37/38: 179−186.

[4] NAKAZAW S, YAZAWA A, JORGENSEN F R A. Simulation of the removal of arsenic during the roasting of

copper concentrate [J]. Metallurgical and Materials Transactions B, 1999, 30: 393−401.

[5] HENAO H, PAREDES I, DIAZ R, ORTIZ J. Pyrometallurgical removal of arsenic from electrostatic precipitators dusts of copper smelting [J]. Journal of Minerals and Materials Characterization and Engineering, 2021, 9: 545−565.

[6] GUO Xue-yi, CHEN Yuan-lin, WANG Qin-meng, WANG Song-song, TIAN Qing-hua. Copper and arsenic substance flow analysis of pyrometallurgical process for copper production [J]. Transactions of Nonferrous Metals Society of China, 2022, 32: 364−376.

[7] YAO Li-wei, MIN Xiao-bo, XU Hui, KE Yong, WANG Yun-yan, LIN Zhang, LIANG Yan-jie, LIU De-gang, XU Qiu-jing, HE Yu-yang. Physicochemical and environmental properties of arsenic sulfide sludge from copper and lead−zinc smelter [J]. Transactions of Nonferrous Metals Society of China, 2020, 30: 1943−1955.

[8] FLORES G A, RISOPATRON C, PEASE J. Processing of complex materials in the copper industry: Challenges and opportunities ahead [J]. JOM, 2020, 72: 3447−3461.

[9] WANG Hong-yang, ZHU Rong, DONG Kai, ZHANG Si-qi, WANG Yun, LAN Xin-yi. Effect of injection of different gases on removal of arsenic in form of dust from molten copper smelting slag prior to recovery process [J]. Transactions of Nonferrous Metals Society of China, 2023, 33: 1258−1270.

[10] ZHANG Hui-bin, HE Yu-zheng, HU Jing-jing, WANG Ya-nan, CAO Hua-zhen, ZHOU Jun, ZHENG Guo-qu. Assessment of selective sequential extraction procedure for determining arsenic partitioning in copper slag [J]. Transactions of Nonferrous Metals Society of China, 2020, 30: 2823−2835.

[11] CHAN B K C, BOUZALAKOS S, DUDENEY A W L. Integrated waste and water management in mining and metallurgical industries [J]. Transactions of Nonferrous Metals Society of China, 2008, 18: 1497−1505.

[12] ARSLAN C, ARSLAN F. Recovery of copper, cobalt, and zinc from copper smelter and converter slags [J]. Hydrometallurgy, 2002, 67: 1−7.

[13] YIN Sheng-hua, WANG Lei-ming, WU Ai-xiang, FREE M L, KABWE E. Enhancement of copper recovery by acid leaching of high-mud copper oxides: A case study at Yangla Copper Mine, China [J]. Journal of Cleaner Production, 2018, 202: 321−331.

[14] SCHLESINGER M E, KING M J, SOLE K C, DAVENPORT W G. Extractive metallurgy of copper [M]. Kidlington, UK: Elsevier Science Ltd, 2011.

[15] SHAO Pin, JIANG Le-peng. Flow and mixing behavior in a new bottom blown copper smelting furnace [J]. International Journal of Molecular Sciences, 2019, 20: 5757.

[16] SHUI Lang, CUI Zhi-xiang, MA Xiao-dong, RHAMDHANI M A, NGUYEN A V, ZHAO Bao-jun. Understanding of bath surface wave in bottom blown copper smelting furnace [J]. Metallurgical and Materials Transactions B, 2016, 47: 135−144.

[17] ZHANG Shan-jia, YANG Yi-shi, STOROZUM M J, LI Hai-ming, CUI Yi-fu, DONG Guang-hui. Copper smelting and sediment pollution in bronze age China: A case study in the Hexi Corridor, Northwest China [J]. Catena, 2017, 156: 92−101.

[18] LI Ming-zhou, TONG Chang-ren, HUANG Jin-di, WANG Jin-liang. Simulated calculation of overall process flow of copper bottom blowing smelting [J]. The Chinese Journal of Process Engineering, 2016, 16: 1028−1037. (in Chinese)

[19] WAN Xing-bang, SUKHOMLINOV D, TASKINEN P, LINDGREN M, MICHALLIK R, JOKILAAKSO A. Arsenic condensation and reaction mechanisms in flash smelting off-gas line conditions [J]. Metallurgical and Materials Transactions B, 2023, 54: 2747−2757.

[20] CHEN Yu-jie, ZHAO Zong-wen, TASKINEN P, LIANG Yan-jie, OUYANG Hong-chuan, PENG Bing, JOKILAAKSO A, ZHOU Song-lin, CHEN Tao, PENG Ning, LIU Hui. Characterization of copper smelting flue dusts from a bottom-blowing bath smelting furnace and a flash smelting furnace [J]. Metallurgical and Materials Transactions B, 2020, 51: 2596−2608.

[21] SOHN H S, FUKUNAKA Y, OISHI T, ASAKI Z, SOHN H Y. Kinetics of As, Sb, Bi and Pb volatilization from industrial copper matte during Ar+O_2 bubbling [J]. Metallurgical and Materials Transactions B, 2004, 35: 651−661.

[22] HALATEK T, SINCZUK-WALCZAK H, JANASIK B, TRZCINKA-OCHOCKA M, WINNICKA R, WASOWICZ W. Health effects and arsenic species in urine of copper smelter workers [J]. Journal of Environmental Science and Health: Part A, 2014, 49: 787−797.

[23] CHEN Chun-lin, ZHANG Ling, JAHANSHAHI S. Thermodynamic modeling of arsenic in copper smelting processes [J]. Metallurgical and Materials Transactions B, 2010, 41: 1175−1185.

[24] SWINBOURNE D R, KHO T S. Computational thermodynamics modeling of minor element distributions during copper flash converting [J]. Metallurgical and Materials Transactions B, 2012, 43: 823−829.

[25] ITAGAKI K, YAZAWA A. Thermodynamic evaluation of distribution behaviour of arsenic in copper smelting [J]. Transactions of the Japan Institute of Metals, 1982, 23: 759−767.

[26] MONTENEGRO V, SANO H, FUJISAWA T. Recirculation of Chilean copper smelting dust with high arsenic content to the smelting process [J]. Materials Transactions, 2008, 49: 2112−2118.

[27] MONTENEGRO V, SANO H, FUJISAWA T. Recirculation of high arsenic content copper smelting dust to smelting and converting processes [J]. Minerals Engineering, 2013, 49: 184−189.

[28] ZHONG Da-peng, LI Lei, TAN Cheng. Separation of arsenic from the antimony-bearing dust through selective oxidation using CuO [J]. Metallurgical and Materials Transactions B, 2017, 48: 1308−1314.

[29] VARTIAINEN A, TASKINEN P, JOKILAAKSO A. Behaviour of impurities on the suspension stage of the

OUTOKUMPU flash smelting furnace [C]//Kellogg International Symposium. Warrendale, PA: TMS, 1991: 45−68.

[30] FENG Qing-mei, WU Yue-hua, JIN Bing-jie, ZHANG Yu-hui, LI Lei. Volatilization mechanization and behaviors of arsenic from high arsenic-containing copper smelting ash by sulfurization roasting [J]. JOM, 2023, 75: 3501−3510.

[31] VYAZOVKIN S, WIGHT C A. Model-free and model-fitting approaches to kinetic analysis of isothermal and nonisothermal data [J]. Thermochimica Acta, 1999, 340/341: 53−68.

[32] KHAWAM A, FLANAGAN D R. Role of isoconversional methods in varying activation energies of solid-state kinetics: II. Nonisothermal kinetic studies [J]. Thermochimica Acta, 2005, 436: 101−112.

[33] KIM B S, KIM E Y, KIM C K, LEE H I, LEE H I, SOHN J S. Kinetics of oxidative roasting of complex copper concentrate [J]. Materials Transactions, 2008, 49: 1192−1198.

[34] OKANIGBE D O, POPOOLA A P I, ADELEKE A A. Thermal analysis and kinetics of the oxidative roasting process of a copper smelter dust [J]. The International Journal of Advanced Manufacturing Technology, 2018, 94: 2393−2400.

[35] CHEN Yu-jie, WANG Yun-yan, PENG Ning, LIANG Yan-jie, PENG Bing. Isothermal reduction kinetics of zinc calcine under carbon monoxide [J]. Transactions of Nonferrous Metals Society of China, 2020, 30: 2274−2282.

[36] PENG Ning. Study on reductive decomposition of zinc ferrite and its application [D]. Changsha: Central South University, 2017. (in Chinese)

[37] CHEN Yu-jie, ZHU Shun, TASKINEN P, PENG Ning, PENG Bing, JOKILAAKSO A, LIU Hui, LIANG Yan-jie, ZHAO Zong-wen, WANG Zhong-bing. Treatment of high-arsenic copper smelting flue dust with high copper sulfate: Arsenic separation by low temperature roasting [J]. Minerals Engineering, 2021, 164: 106796.

[38] HU Gui-lin, DAM-JOHANSEN K, WEDEL S, HANSEN J P. Decomposition and oxidation of pyrite [J]. Progress in Energy and Combustion Science, 2006, 32: 295−314.

[39] DUNN J G, GINTING A R, O'CONNOR B. A thermoanalytical study of the oxidation of chalcocite [J]. Journal of Thermal Analysis, 1994, 41: 671−686.

[40] JORGENSEN F R A, MOYLE F J. Phases formed during the thermal analysis of pyrite in air [J]. Journal of Thermal Analysis, 1982, 25: 473−485.

[41] FAN Bo-wen. Heating phases of pyrite and their magnetic property and mechanism [D]. Chengdu: Chengdu University of Technology, 2011. (in Chinese)

[42] PÉREZ-FONTES S E, PÉREZ-TELLO M, PRIETO-LÓPEZ L O, BROWN F, CASTILLÓN-BARRAZA F. Thermoanalytical study on the oxidation of sulfide minerals at high temperatures [J]. Mining, Metallurgical & Exploration, 2007, 24: 275−283.

[43] ZHAO Zong-wen, WANG Zhong-bing, PENG Ning, PENG Bing, LIANG Yan-jie, QU Sheng-li, DONG Zhun-qing, ZENG Wei-zhi. Copper behavior and fayalite microstructure changes influenced by Cu_2O dissolution [J]. JOM, 2019, 71: 2891−2898.

[44] NAZARI A M, RADZINSKI R, GHAHREMAN A. Review of arsenic metallurgy: Treatment of arsenical minerals and the immobilization of arsenic [J]. Hydrometallurgy, 2017, 174: 258−281.

[45] AHOKAINEN T, JOKILAAKSO A, TASKINEN P, KYTO M. A new advanced CFD model for flash smelting and converting processes [C]//International Symposium on Sulfide Smelting. Warrendale, PA: TMS, 2006: 529−543.

[46] JOKILAAKSO A, SUOMINEN R, HACKMAN H, TASKINEN P, LILIUS K. The behaviour of tetrahedrite in simulated suspension smelting conditions [C]//Center for Pyrometallurgy Conference. Rolla, MO, USA: University of Missouri-Rolla, 1988: 201−213.

[47] JOKILAAKSO A, TASKINEN P, SUOMINEN R, LILIUS K. Antimony in flash smelting simulation experiments. Part 2: The behaviour of a medium antimony concentrate [J]. Scandinavian Journal of Metallurgy, 1994, 23: 54−61.

[48] WINKEL L, WOCHELE J, LUDWIG C, ALXNEIT I, STURZENEGGER M. Decomposition of copper concentrates at high-temperatures: An efficient method to remove volatile impurities [J]. Minerals Engineering, 2008, 21: 731−742.

[49] SEITKAN A, REDFERN S A T. Processing double refractory gold-arsenic-bearing concentrates by direct reductive melting [J]. Minerals Engineering, 2016, 98: 286−302.

[50] HAGA K, ALTANSUKH B, SHIBAYAMA A. Volatilization of arsenic and antimony from tennantite/tetrahedrite ore by a roasting process [J]. Materials Transactions, 2018, 59: 1396−1403.

[51] BRUCKARD W J, DAVEY K J, JORGENSEN F R A, WRIGHT S, BREW D R M, HAQUE N, VANCE E R. Development and evaluation of an early removal process for the beneficiation of arsenic-bearing copper ores [J]. Minerals Engineering, 2010, 23: 1167−1173.

高砷铜熔炼炉料在悬浮熔炼过程中的行为

陈玉洁[1]，梁彦杰[2,3]，刘 恢[2,3]，Pekka TASKINEN[4]，
Ari JOKILAAKSO[4]，董准勤[5]，王忠兵[6]，陈 涛[5]

1. 南阳理工学院 生物与化学工程学院，南阳 473000；
2. 中南大学 冶金与环境学院，长沙 410083；
3. 国家重金属污染防治工程技术研究中心，长沙 410083；
4. School of Chemical Engineering, Aalto University, Espoo, 00076, Finland；
5. 山东恒邦冶炼股份有限公司，烟台 264000；
6. 南昌航空大学 环境与化学工程学院，南昌 330063

摘 要：通过在氮气和空气气氛下，将高砷铜熔炼原料混合物在 500~900 ℃下煅烧 0~20 s，对铜闪速熔炼的悬浮阶段展开研究。采用化学分析方法测定水淬煅烧产物中铜、铅、锌、砷和硫的富集行为。炉料以黄铁矿和黄铜矿为主要矿物，约 55% (质量分数)的砷以砷黝铜矿形式存在。通过热重和质谱联用技术，研究原料的热稳定性及煅烧过程中 S_2 和 SO_2 的生成情况，并对选定的单一硫化物的热力学行为进行研究，为实验结果提供参考依据。结果表明，相较于空气气氛，惰性气氛更有利于砷的释放，这是因为在空气中硫化物的氧化产物会捕获释放出的气态砷。动力学分析表明，三级化学反应机理和三维扩散模型分别被确定为惰性气氛和空气气氛下砷挥发的最优机理函数。

关键词：复杂精矿；铜熔炼；闪速熔炼；挥发；动力学模型

(Edited by Xiang-qun LI)